

High Entropy Approach to Engineer Strongly Correlated Functionalities in Manganites

Abhishek Sarkar,* Di Wang,* Mohana V. Kante, Luis Eiselt, Vanessa Trouillet, Gleb Iankevich, Zhibo Zhao, Subramshu S. Bhattacharya, Horst Hahn, and Robert Kruk*

Technologically relevant strongly correlated phenomena such as colossal magnetoresistance (CMR) and metal-insulator transitions (MIT) exhibited by perovskite manganites are driven and enhanced by the coexistence of multiple competing magneto-electronic phases. Such magneto-electronic inhomogeneity is governed by the intrinsic lattice-charge-spin-orbital correlations, which, in turn, are conventionally tailored in manganites via chemical substitution, charge doping, or strain engineering. Alternately, the recently discovered high entropy oxides (HEOs), owing to the presence of multiple-principal cations on a given sub-lattice, exhibit indications of an inherent magneto-electronic phase separation encapsulated in a single crystallographic phase. Here, the high entropy (HE) concept is combined with standard property control by hole doping in a series of single-phase orthorhombic HE-manganites (HE-Mn), $(\text{Gd}_{0.25}\text{La}_{0.25}\text{Nd}_{0.25}\text{Sm}_{0.25})_{1-x}\text{Sr}_x\text{MnO}_3$ ($x = 0-0.5$). High-resolution transmission microscopy reveals hitherto-unknown lattice imperfections in HEOs: twins, stacking faults, and missing planes. Magnetometry and electrical measurements infer three distinct ground states—insulating antiferromagnetic, unpercolated metallic ferromagnetic, and long-range metallic ferromagnetic—coexisting or/and competing as a result of hole doping and multi-cation complexity. Consequently, CMR $\approx 1550\%$ stemming from an MIT is observed in polycrystalline pellets, matching the best-known values for bulk conventional manganites. Hence, this initial case study highlights the potential for a synergetic development of strongly correlated oxides offered by the high entropy design approach.

1. Introduction

The interplay between spin, orbital, and charge order in strongly correlated electron systems underlies emergent phenomena such as superconductivity, colossal magnetoresistance (CMR), metal-insulator transitions (MIT), etc., which are of immense fundamental and technological interest.^[1-3] The perovskite type rare-earth (RE) manganites and their chemical hole (h^+) doped variants, $\text{RE}_{1-x}\text{A}_x\text{MnO}_3$, are an important class of materials exhibiting multiple strongly correlated effects like MIT, CMR, charge-ordering (CO), and orbital-ordering (OO).^[2,4] The properties exhibited by the $\text{RE}_{1-x}\text{A}_x\text{MnO}_3$ systems are primarily governed by two competing magneto-electronic states: one is the ferromagnetic (FM) metallic (FM-M) state stemming from double-exchange (DE) $\text{Mn}^{4+}\text{-O}^{2-}\text{-Mn}^{3+}$ interactions, while the other one is the antiferromagnetic (AF) insulating state (AF-I) originating from superexchange (SE) $\text{Mn}^{3+}\text{-O}^{2-}\text{-Mn}^{3+}$ or $\text{Mn}^{4+}\text{-O}^{2-}\text{-Mn}^{4+}$ interactions and related CO of Mn^{3+} and Mn^{4+} .^[5,6] Likewise, FM-I and AF-M states are the result

A. Sarkar, L. Eiselt, H. Hahn
KIT-TUD Joint Research Laboratory Nanomaterials – Technische
Universität Darmstadt
Otto-Berndt-Str. 3, 64287 Darmstadt, Germany
E-mail: abhishek.sarkar@kit.edu

A. Sarkar, D. Wang, M. V. Kante, G. Iankevich, Z. Zhao, H. Hahn, R. Kruk
Institute of Nanotechnology
Karlsruhe Institute of Technology
Hermann-von-Helmholtz-Platz 1, 76344 Eggenstein-Leopoldshafen,
Germany
E-mail: di.wang@kit.edu; robert.kruk@kit.edu

 The ORCID identification number(s) for the author(s) of this article can be found under <https://doi.org/10.1002/adma.202207436>.

© 2022 The Authors. Advanced Materials published by Wiley-VCH GmbH. This is an open access article under the terms of the Creative Commons Attribution-NonCommercial-NoDerivs License, which permits use and distribution in any medium, provided the original work is properly cited, the use is non-commercial and no modifications or adaptations are made.

DOI: 10.1002/adma.202207436

D. Wang, V. Trouillet
Karlsruhe Nano Micro Facility (KNMFI)
Karlsruhe Institute of Technology (KIT)
Hermann-von-Helmholtz-Platz 1, 76344 Eggenstein-Leopoldshafen,
Germany

V. Trouillet
Institute for Applied Materials (IAM-ESS)
Karlsruhe Institute of Technology (KIT)
Hermann-von-Helmholtz-Platz 1, 76344 Eggenstein-Leopoldshafen,
Germany

G. Iankevich, H. Hahn
Institute for Quantum Materials and Technologies (IQMT)
Karlsruhe Institute of Technology
Hermann-von-Helmholtz-Platz 1, 76344 Eggenstein-Leopoldshafen,
Germany

S. S. Bhattacharya
Nanofunctional Materials Technology Centre (NFMTC)
Department of Metallurgical and Materials Engineering
Indian Institute of Technology Madras
Chennai 600036, India

of competition between the elementary SE and DE magneto-electronic interactions. The FM-I occurs when the percolation of FM-M state is restricted by the AF-I state, while the AF-M is believed to arise from FM-M planes with uniform OO. In addition, manganites show prominent electron-lattice coupling, a part of which is driven by the Jahn–Teller ($J-T$) effect originating from Mn^{3+} (in six-fold coordination) that results in lattice distortion and electron localization.^[7] Therefore, one of the main directions of research on RE-manganites is the control of electron-lattice-magnetic coupling.^[2] The most commonly used approach to control the charge state of Mn and engineer the crystal structure is the chemical substitution on the RE-site.

The chemical (aliovalent) charge doping on the RE-site, on one hand, directly impacts the Mn-band filling via change in Mn oxidation state resulting in different magneto-electronic ground states (such as AF vs. FM and insulating vs conducting). On the other hand, the change in the RE-site ionic radii achieved via elemental substitution (isovalent as well as aliovalent) affects the one-electron charge carrier bandwidth (W) governing the electron interionic transfer.^[4,8] For instance, $La_{1-x}Sr_xMnO_3$ is the well-known case of a large W system, where the itinerant electronic states are preferred and the metallic state (FM-M or AF-M) spans over a wide range of h^+ doping.^[4,9] In fact, paramagnetic-metallic (PM-M) is an evident state at certain h^+ concentrations.^[4,9] In contrast, $La_{1-x}Ca_xMnO_3$, despite the fact that Ca^{2+} leads to a similar Mn-band filling like that with Sr^{2+} doping, results in an intermediate W due to differences in the ionic radii. As a result, the metallic state is comparatively suppressed in $La_{1-x}Ca_xMnO_3$. A direct impact of this suppression is evident from the significantly higher CMR values exhibited by $La_{1-x}Ca_xMnO_3$ compared to $La_{1-x}Sr_xMnO_3$. Finally, an extreme case narrow- W system is $Pr_{1-x}Ca_xMnO_3$, where the system tends to stay in an insulating state almost over the entire h^+ dopant regime.^[4] Overall, both the filling of the Mn band and the change in W resulting from chemical substitution on the RE-site strongly affect the competition among the different magneto-electronic phases in manganites by controlling the kinetic energy of the conduction electrons. Importantly, the competing interactions between the primary magnetically ordered states (FM-M, FM-I, AF-I, and AF-M) lead to magneto-electronic inhomogeneity and as a result make the properties of these materials extremely sensitive to external parameters, such as magnetic field, temperature, or pressure.^[1,3,10] Hence, the RE-site chemical substitution is considered the most fundamental tool to tune functionalities of perovskite manganites, such as MIT and CMR.

The recently introduced “high entropy (HE)” materials provide a natural environment for the magneto-electronic phase competition/coexistence by the virtue of their extreme chemical complexity.^[11–15] The HE design approach in oxides is based on incorporation of multiple cations in near-equimolar ratio in a given cation sub-lattice.^[11,12,16,17] Despite the compositional complexity stemming from the presence of multiple principal cations, high entropy oxides (HEOs) crystallize as single-phase solid solutions.^[11–13] The term HE is used and the same nomenclature has been adapted in this study following the well-known HE alloys. This is because these systems possess considerably higher configurational entropy (as

dictated by the Boltzmann's equation) compared to their conventional counterparts.^[11–15,18] HEOs offer the possibility to explore the unraveled composition space close to the center of multinary oxide phase diagrams for potentially unique properties. The field of HEOs has rapidly grown to include several compositions and crystallographic structures.^[11,12] Multiple studies already highlight their improved functionalities, such as enhanced energy storage capability, high catalytic activity, suppressed thermal conductivity, etc.^[19–25] The magnetic properties of single-phase HEOs are of interest as significant magnetic phase separation manifesting itself through the intrinsic exchange bias has been reported.^[26–28] Although pinpointing the exact origins of the magnetic phase separation is challenging, it is hypothesized that varying exchange interactions due to the presence of multiple cations with different spin-electronic states, atomic-scale deviation from a complete cationic disorder, and locally varying metal–oxygen–metal bond angles can result in such separation.^[26,28,29] Consequently, the presence of competing magneto-electronic states and observed magnetic phase separation in HEOs inspire an idea of a possible unification of the HE and strong-correlated electrons in one system.

Motivated by the aforementioned connection, here, we aim to extend the HE-based approach to the design of strongly correlated systems by studying a series of h^+ doped high-entropy manganites (HE-Mn). To date, there are three reports available on HE-Mn.^[30–32] In the first report, the studied HE-Mn system exhibited a single-phase solid solution only at elevated temperatures, as indicated by the operando high-temperature X-ray diffraction (XRD) measurements.^[30] In the later studies, composition modulation allowed the stabilization of phase-pure HE-Mn at room temperature.^[31,32] Their transport properties were then investigated, which, along with their enhanced thermal stability, highlight the potential of HE-Mn for use as cathode materials in solid oxide fuel cells (SOFCs).^[31,32] The present study, on the other hand, focuses on $(Gd_{0.25}La_{0.25}Nd_{0.25}Sm_{0.25})_{1-x}Sr_xMnO_3$ ($x = 0-0.5$) based compositions of HE-Mn. Detailed structural investigations have been performed to evaluate their phase compositions and accompanying lattice imperfections. HE-Mn exhibit a complex magneto-electronic phase-space with distinct competing/coexisting ground states. The possible utilization of the HE approach applied to the strongly correlated systems is highlighted by both the observed prominent magneto-electronic phase separation and the substantial CMR effect.

2. Results and Discussion

2.1. Structure, Phase Composition, Elemental Distribution, Lattice Defects, and Mn Valence States in $(Gd_{0.25}La_{0.25}Nd_{0.25}Sm_{0.25})_{1-x}Sr_xMnO_3$

In this section, we combine X-ray diffraction (XRD), high-resolution (scanning) transmission electron microscopy (HR-STEM), electron energy loss spectroscopy (EELS), energy dispersive spectroscopy (EDS) and X-ray photoelectron spectroscopy (XPS) to investigate the global and local structural features of HE-Mn, which are crucial for elucidating their magneto-electronic functionalities.

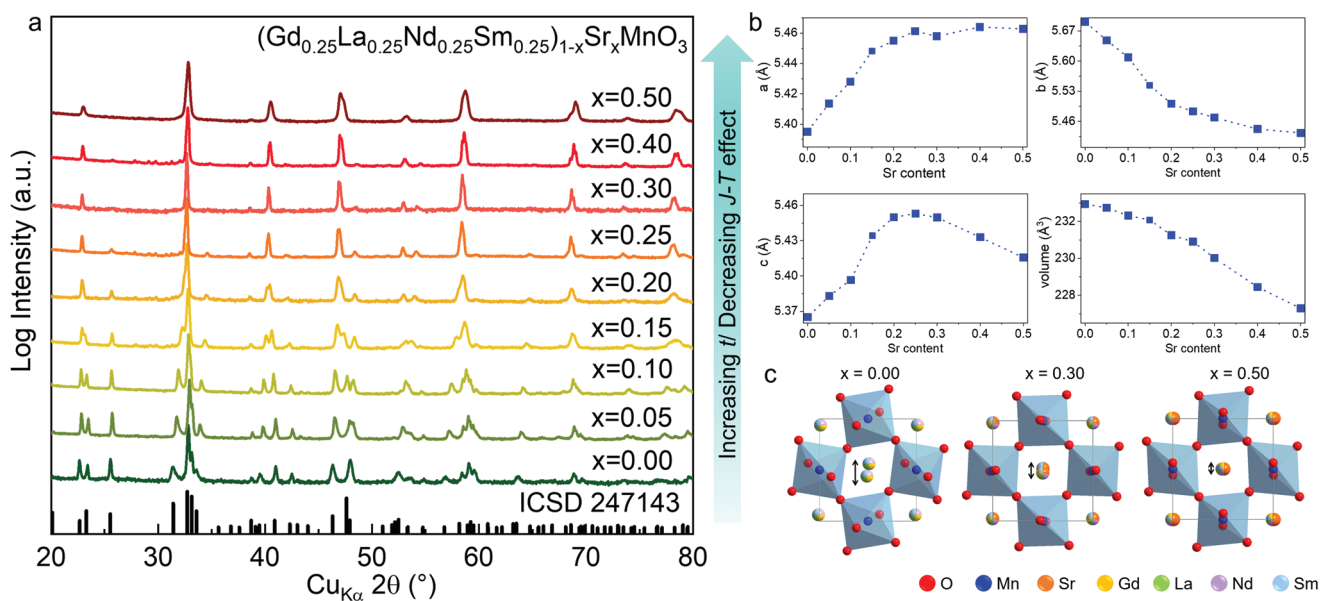


Figure 1. Crystal structure and phase compositions of $(\text{Gd}_{0.25}\text{La}_{0.25}\text{Nd}_{0.25}\text{Sm}_{0.25})_{1-x}\text{Sr}_x\text{MnO}_3$ ($x = 0-0.5$). a) XRD patterns indicating that all the systems crystallize in a single-phase orthorhombic ($Pbnm$) structure. The t and $J-T$ effect stand for Goldschmidt tolerance factor and Jahn–Teller effect, respectively. b) The variation in the lattice parameters and cell volume obtained from Rietveld refinement is shown as a function of Sr content. c) The structural schematics (using the information obtained from the Rietveld refinement) along the $Pbnm$ c -axis show a gradual decrease in the orthorhombic distortion upon Sr addition.

2.1.1. XRD and Rietveld Analysis

Figure 1a presents the XRD patterns of all studied compositions. The analysis indicates that all the compositions crystallized in single-phase orthorhombic structures ($Pbnm$) despite the high chemical complexity. Rietveld refinement of the XRD patterns is provided in Figure S1 (Supporting Information). The obtained lattice parameters and the cell volumes are shown in Figure 1b. The Goldschmidt tolerance factor (t), which is defined using Equation 1 (for a general ABO_3 perovskite), increases with increasing amount of Sr doping

$$t = \frac{r_A + r_O}{\sqrt{2}(r_B + r_O)} \quad (1)$$

where r_A and r_B are the ionic radii of the cations occupying the A-site and B-site (Mn), respectively, and r_O is the radius of the oxygen ion. In the case of the disordered A-site, the average ionic radii is considered.

In addition, the $J-T$ effect also decreases (more details in the following paragraphs) with increasing Sr^{2+} doping. This is reflected in the XRD patterns where a decrease in the orthorhombic nature of the sample is evident from gradual lowering of the super-structure reflections and merging of a , b , $c/\sqrt{2}$ parameters upon Sr^{2+} doping. In fact, the XRD patterns of samples with $x = 0.40$ and 0.50 , appear more cubic rather than orthorhombic. However, closer inspection of the peak shapes and refinement of the XRD patterns indicate that these samples are still single-phase orthorhombic. The structural information obtained from the Rietveld refinements is pictorially represented in Figure 1c, which further indicates the lowering degree of orthorhombicity upon increasing the amount of Sr^{2+} doping.

2.1.2. HR-STEM, EDS, EELS, and XPS

In order to gain deeper insight about the crystal structure, chemical homogeneity, and oxidation state of Mn, HR-STEM has been performed on four systems, $x = 0, 0.2, 0.3$, and 0.5 . The HR-STEM micrographs and corresponding fast Fourier transform (FFT) images of $x = 0$ and 0.5 are shown in Figure 2a,b, while the data for $x = 0.2$ and 0.3 are presented in Figure S2 (Supporting Information). These data along with additional HRTEM and HR-STEM images acquired at several other regions with various zone axes for each of these samples, confirm the presence of single-phase orthorhombic perovskite in all these studied systems. For the $x = 0$ sample, the structural modulation stemming from the orthorhombic distortion is prominent as indicated by the shifted lattice position of B-site (Mn) in the neighboring atomic planes perpendicular to the c -axis (Figure 2a). In contrast, a significant decrease in the orthorhombic distortion can be observed in the $x = 0.5$ system (Figure 2b). Figure 2c,d present the high-angle annular dark-field (HAADF) image and the corresponding atomically resolved elemental distribution maps for $x = 0$ and $x = 0.5$. A homogenous distribution of the rare-earth cation (and Sr for $x = 0.5$) on the A-site (RE) sub-lattice along with presence of Mn on the B-site sub-lattice, without any observable concentration fluctuation at the atomic length scales, can be confirmed. The obtained chemical distribution strengthens the claim of structural homogeneity in the HE-Mn.

In order to evaluate the oxidation state of Mn, EELS measurements on the Mn $L_{2,3}$ -edges and the O K -edges have been performed (Figure S3, Supporting Information). The Mn L -edge spectra show two characteristic features stemming from Mn L_3 (≈ 643 eV) and Mn L_2 (≈ 644 eV) edges.^[33,34] The O K -edge spectra

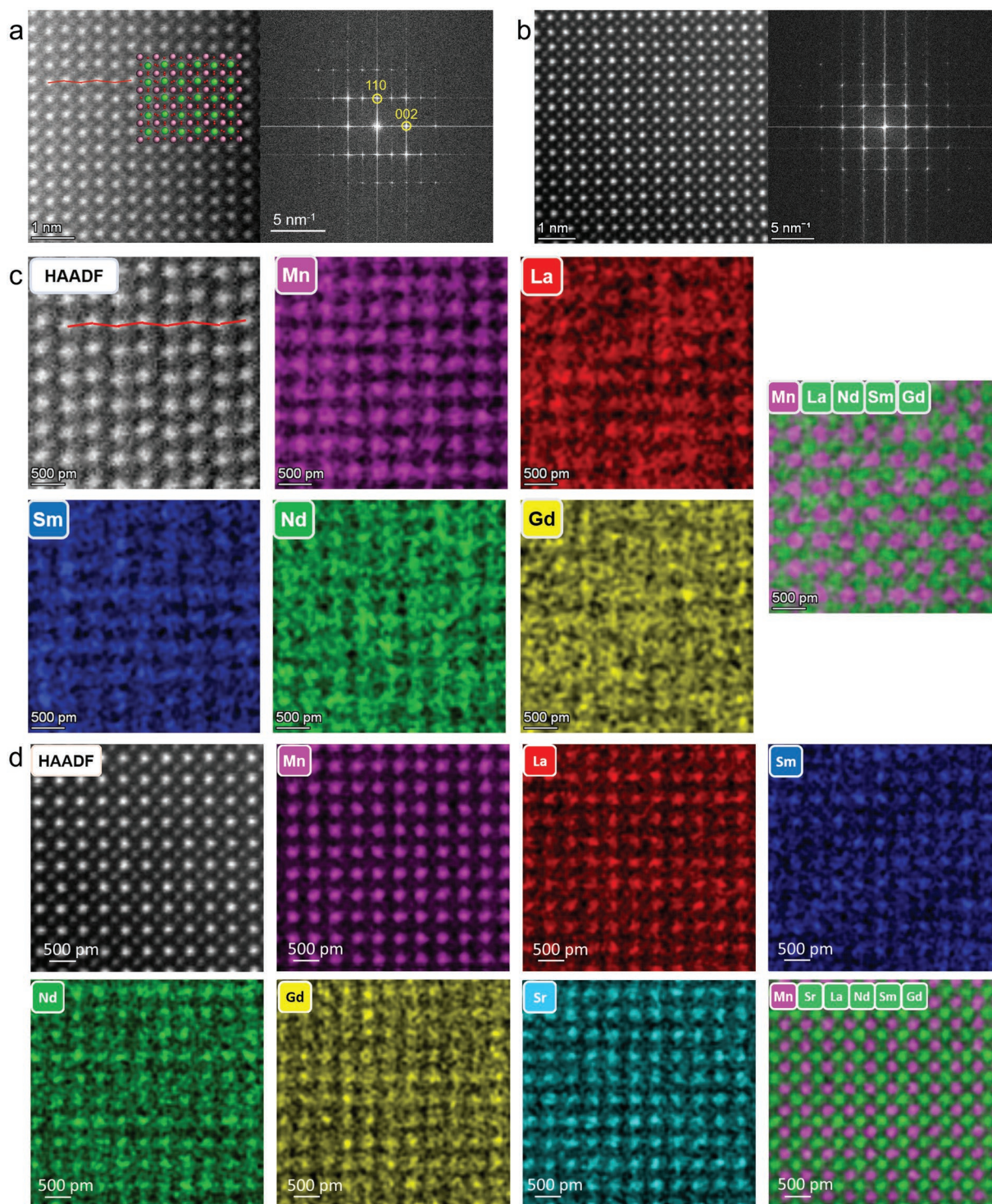


Figure 2. Atomic resolution HAADF-STEM micrographs and EDS elemental maps for representative $x = 0.0$ and 0.5 systems. a,b) HAADF-STEM micrographs and corresponding FFTs from the $[110]$ zone axis of $x = 0.0$ (a) and 0.5 (b) systems indicate phase-pure $Pbnm$ structure in both the systems. A decrease in the degree of the orthorhombic distortion is observed in the case of the $x = 0.5$. c,d) The corresponding elemental distribution maps for $x = 0.0$ (c) and 0.5 (d) systems show that all the RE cations and Sr homogeneously occupy the A-site sub-lattice while Mn occupies the B-site sub-lattice, without any observable elemental fluctuations even at the atomic length scales.

show three main features at ≈ 530 , 536 , and 543 eV, which originate from hybridization of O^{2-} with the relevant metal cation (Mn or RE).^[33,34] The feature at ≈ 543 eV can be attributed to

hybridization of O^{2-} with Mn $4sp$ (hybridized) orbitals, while the one at ≈ 536 eV is related to hybridization with RE $5d$ and Sr $4d$ orbitals. Finally, the important one at ≈ 530 eV is related to the

hybridization with the Mn 3d orbitals. The change in the oxidation state of Mn can be extracted from the integrated area ratio of the Mn L_3 to Mn L_2 edges (L_3/L_2 ratio) after subtracting the continuum excitations and the difference in the positions (ΔE) between the Mn 3d feature (≈ 530 eV) and the RE 5d/Sr 4d feature (≈ 536 eV). A decrease in L_3/L_2 ratio or an increase in the ΔE signifies an increasing Mn oxidation state.^[33,34] The change in the L_3/L_2 ratio and ΔE as a function of Sr²⁺ doping shown in Figure S4 (Supporting Information) unambiguously confirms the premise that increasing the amount of Sr²⁺ doping results in more Mn⁴⁺. In fact, the expected difference between oxidation state Mn for $x = 0.5$ and $x = 0$ is $\approx +0.5$, which is also in good agreement with the amount of h^+ doping. The effective valence states of Mn obtained in $x = 0$ and $x = 0.5$ are $\approx 3+$ and $\approx 3.5+$, respectively. Nevertheless, it should be noted that although the L_3/L_2 ratio and ΔE are reliable qualitative parameters, they provide only semi-quantitative estimations of the real Mn oxidation state. Hence, from the EELS study, it can only be concluded that the relative amount of Mn⁴⁺:Mn³⁺ increases with h^+ doping and the extent of increase agrees well with the amount of h^+ doping.

XPS measurements on $x = 0, 0.2, 0.3,$ and 0.5 and two reference standards (MnO₂ and Mn₃O₄) have been performed to

further ascertain the increase in the oxidation state of Mn upon h^+ doping. The results of the XPS study and Mn 3s spectral analysis are provided in Figure S5 (Supporting Information) and the related discussion section. The trend observed from the surface-sensitive XPS analysis in combination with the volume sensitivity of EELS provides a deeper insight into the change in oxidation state of Mn in the HE-Mn upon Sr doping. Consequently, these indicate the lowering of the $J-T$ effect with an increasing amount of h^+ doping which is also reflected from the global lowering of the orthorhombicity observed from the Rietveld analysis.

Apart from the observation of a single orthorhombic phase, however, with higher symmetry close to cubic structure, three different kinds of lattice defects were noticeably observed in different regions of (Gd_{0.25}La_{0.25}Nd_{0.25}Sm_{0.25})_{0.5}Sr_{0.5}MnO₃. It should be noted that these defects were not evident in the other probed samples, i.e., $x = 0, 0.2,$ and 0.3 . The first kind of defects were twins, clearly observed in the HR-STEM image and its corresponding FFT shown in Figure 3a,b. The second kind of defect that was observed is an entire missing Mn–O plane, as revealed by the integrated differential phase contrast (iDPC) image in Figure 3c. The third kind of defect that could

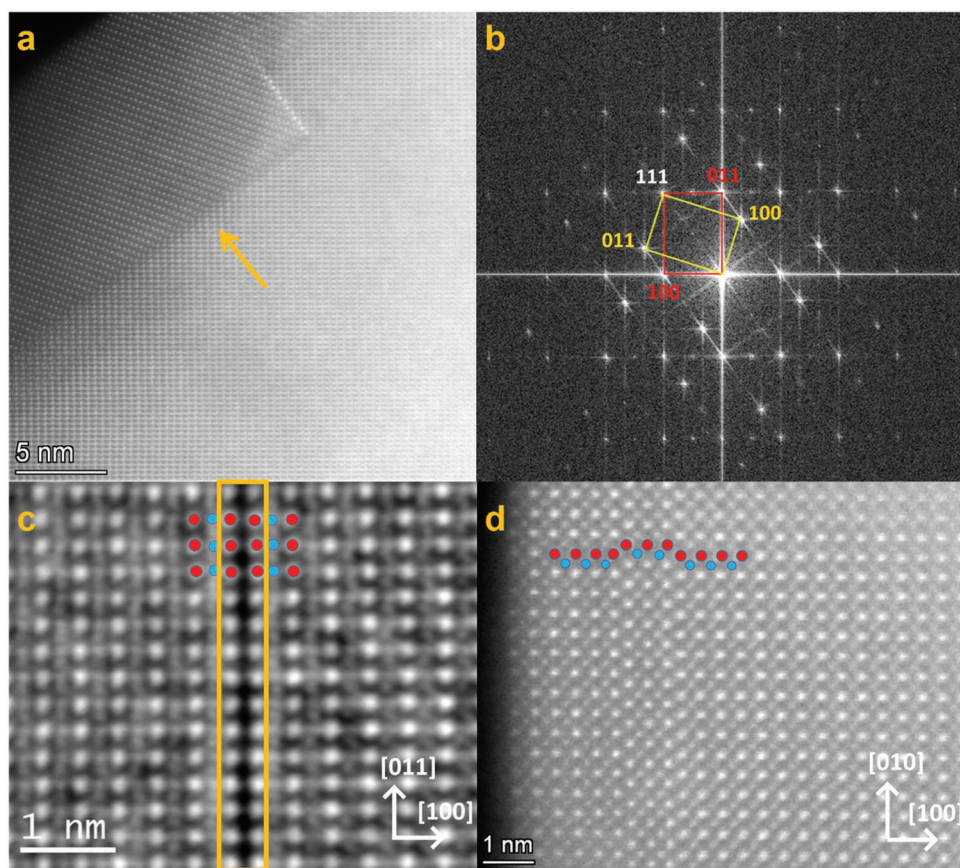


Figure 3. Lattice imperfections in (Gd_{0.25}La_{0.25}Nd_{0.25}Sm_{0.25})_{0.5}Sr_{0.5}MnO₃. a,b) Presence of twinning with a clear twin boundary is confirmed from the STEM micrograph and the corresponding FFT pattern. In c and d, the red balls indicate the RE cations while the blue balls indicate the Mn ions. c) Integrated differential phase contrast (iDPC) image indicates a missing Mn–O plane in the system, with either side of the missing plane showing a continuity of the periodicity and perfect lattice structure. d) If a horizontal line is drawn across the STEM micrograph, then a defect similar to a stacking fault can be observed. The mismatch in the stacking sequence arises from a region with a width of two unit cells. The indices in the FFT and the crystallographic directions are indicated according to the corresponding pseudo-cubic crystal structure of (Gd_{0.25}La_{0.25}Nd_{0.25}Sm_{0.25})_{0.5}Sr_{0.5}MnO₃.

be observed in the system is identical to a stacking fault. When viewed along the edge of the pseudo-cubic structural unit, a region with a width of two unit cells shifts by half the diagonal of the cube. Consequently, the RE and Sr ions align with Mn ions and vice versa corresponding to a perfect crystal, as shown in Figure 3d and Figure S6 (Supporting Information).

It can be roughly estimated that these three aforementioned defects occur in $\approx 20\%$ of the probed sample regions. So, these initial results highlight subtle lattice imperfections in $(\text{Gd}_{0.25}\text{La}_{0.25}\text{Nd}_{0.25}\text{Sm}_{0.25})_{0.5}\text{Sr}_{0.5}\text{MnO}_3$. It should be noted that these three different defects observed here have never been reported for any other HEO system. Nevertheless, a recent dedicated TEM study has shown an enhanced degree of dislocation densities in pyrochlore-HEO systems.^[35] Hence, probing of unique and possibly enhanced lattice imperfections might be an interesting research avenue for HEOs in general. In addition, the defects observed here can also have a decisive influence on the properties, for instance, the missing plane (Mn–O) and the stacking fault-like feature are likely to impact the Mn–O–Mn bonding characteristics that govern exchange interactions in manganites. Studies on bilayer perovskites have shown that the variation in the stacking sequence can result in change of the electronic conductivity as well as magnetic transition temperature.^[36–38] Hence, it can be expected that these defects observed in $(\text{Gd}_{0.25}\text{La}_{0.25}\text{Nd}_{0.25}\text{Sm}_{0.25})_{0.5}\text{Sr}_{0.5}\text{MnO}_3$ can influence its magnetic and electronic properties. Nevertheless, any reliable connection with the properties requires exact quantification of each kind of these defects, which necessitates future dedicated TEM studies. Furthermore, a speculation regarding the effect of these defects on the properties cannot reliably or unequivocally be drawn as, to the best of our knowledge, none of these defects (missing Mn–O plane or stacking faults) have been reported earlier for any bulk perovskite RE–Mn based system. Thus, additional theoretical studies are required to explain the changes in magnetic interactions resulting from these lattice defects. Another possible future work will be to clarify the origin of the lattice imperfections in $(\text{Gd}_{0.25}\text{La}_{0.25}\text{Nd}_{0.25}\text{Sm}_{0.25})_{0.5}\text{Sr}_{0.5}\text{MnO}_3$. This may allow the further optimization of the concentration of defects in $(\text{Gd}_{0.25}\text{La}_{0.25}\text{Nd}_{0.25}\text{Sm}_{0.25})_{0.5}\text{Sr}_{0.5}\text{MnO}_3$ with an aim to tune their functional properties.

On the whole, from the XRD, HR-TEM, EDS, and EELS studies we conclude that all the studied systems, $(\text{Gd}_{0.25}\text{La}_{0.25}\text{Nd}_{0.25}\text{Sm}_{0.25})_{1-x}\text{Sr}_x\text{MnO}_3$ ($x = 0, 0.05, 0.1, 0.15, 0.20, 0.25, 0.30, 0.40, 0.50$), crystallize in a single phase orthorhombic structure with homogenous distribution of the respective cations on their given sub-lattices (RE and Sr on the A-site and Mn on the B-site). The analyses show an increase in the amount of Mn^{4+} and a corresponding decrease in J – T effect and the degree of orthorhombic distortion upon increasing amount of Sr^{2+} doping. Furthermore, $(\text{Gd}_{0.25}\text{La}_{0.25}\text{Nd}_{0.25}\text{Sm}_{0.25})_{0.5}\text{Sr}_{0.5}\text{MnO}_3$ exhibit three different kinds of lattice imperfections: twins, stacking faults and missing Mn–O planes.

2.2. Magnetic and Electronic Properties of $(\text{Gd}_{0.25}\text{La}_{0.25}\text{Nd}_{0.25}\text{Sm}_{0.25})_{1-x}\text{Sr}_x\text{MnO}_3$

In this section, we discuss the results obtained from magnetometry (Figures 4 and 5) and electronic measurements

(Figure 6) of the HE–Mn. Consequently, we construct the complex magneto-electronic phase diagram (Figure 7) of HE–Mn along with graphical representations of the identified magneto-electronic ground states.

2.2.1. Magnetic Properties of $(\text{Gd}_{0.25}\text{La}_{0.25}\text{Nd}_{0.25}\text{Sm}_{0.25})_{1-x}\text{Sr}_x\text{MnO}_3$

The temperature-dependent magnetization (M – T), i.e., the zero-field cooled (ZFC) and field cooled (FC) measurements, for all the nine systems are plotted in Figure 4a–c. The magnetic field-dependent magnetization plots (M – H) at different temperatures ($T = 5, 30, 100, \text{ and } 300 \text{ K}$) for four samples $x = 0.05, 0.30, 0.40,$ and 0.50 are presented in Figure 5, while the M – H plots for the remaining systems are shown in Figure S7 (Supporting Information). The transition temperatures are estimated from the derivative (dM/dT_{FC}) of the FC curves, while the ground states are inferred from the combination of the ZFC, FC, dM/dT_{FC} features and analysis of the saturated Mn magnetic moments obtained from the (M – H) loops collected at different temperatures. The two fundamental characteristics obtained from the magnetic analysis, i.e., the magnetic transition temperatures and the magnetic ground states, are presented in the form of the magneto-electronic phase diagram shown in Figure 7. In the following sections, the magnetic properties of HE–Mn are discussed in detail.

As mentioned earlier, the strong Mn–O–Mn exchange interactions are the dominant ones in manganites, where the RE ion size influences the strength of the exchange interaction by affecting the angle of the Mn–O–Mn bonds and bandwidth W . However, apart from that, the effect of RE cations in $(\text{Gd}_{0.25}\text{La}_{0.25}\text{Nd}_{0.25}\text{Sm}_{0.25})_{1-x}\text{Sr}_x\text{MnO}_3$ with (high) paramagnetic (PM) moments (such as Gd^{3+} : $8 \mu\text{B}$, Nd^{3+} : $3.5 \mu\text{B}$ and Sm^{3+} : $1.5 \mu\text{B}$) should also be considered, especially at low temperatures, while extracting the magnetic moments of the Mn sub-lattice from the M – H curves. In addition, the constituent RE cations, also couple AF with the Mn spins (RE–O–Mn) at low temperatures, indicated by the secondary features indexed as T_{RE} in the M – T curves (Figure 4). Furthermore, the RE sub-lattice itself can get ordered via RE–O–RE interactions. However, this typically occurs at even lower temperatures and, thus, remains largely unnoticed. Importantly, the relative RE PM contribution to the M – H plots gets lowered with increasing amount of non-magnetic Sr^{2+} on the A-site sub-lattice.

The ZFC, FC and dM/dT_{FC} curves for the low Sr doping level, i.e., compositions with $x = 0, 0.05,$ and $0.10,$ are shown in Figure 4a–c. The characteristic cusps observed in the ZFC curves match with the global minima of dM/dT_{FC} . This indicates a PM to AF transition, with the Néel temperatures T_{N} being the maxima of the cusps observed in the ZFC (that is equal to the minima of dM/dT_{FC}). Furthermore, in all the cases the FC branches show a drop in the magnetization at $\approx 25 \text{ K}$ indicated by T_{RE} arising from the RE–O–Mn AF coupling. The significant splitting between the ZFC and the FC curves, with the FC curve appearing more like expected in FM affirms the canting of the AF Mn spins leading to small net FM moments. As mentioned earlier, AF ordering in lower h^+ doping stems from SE–AF interactions between Mn^{3+} –O– Mn^{3+} . Furthermore, the SE–AF coupling can also have an asymmetric component due to

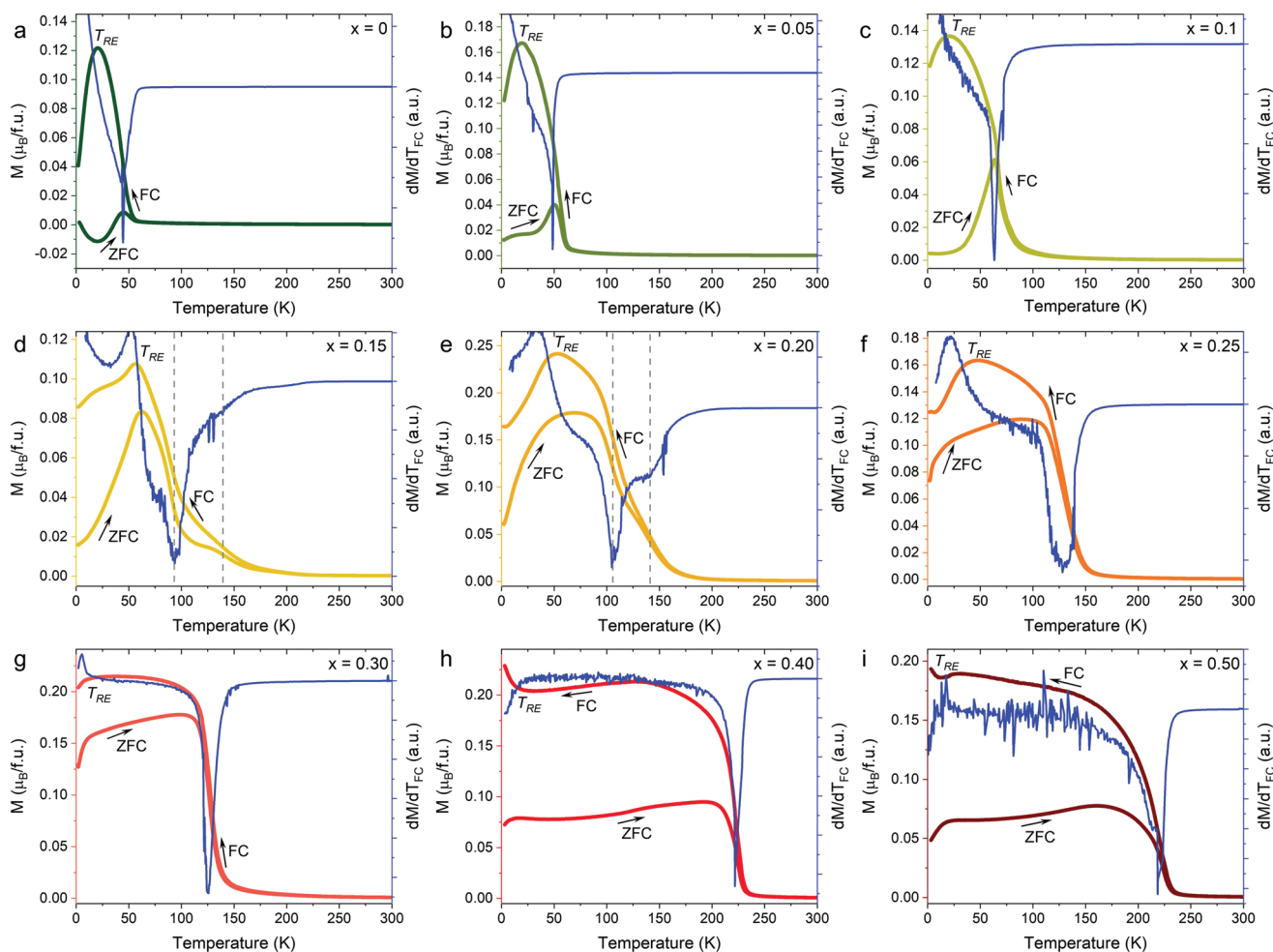


Figure 4. Magnetization of $(\text{Gd}_{0.25}\text{La}_{0.25}\text{Nd}_{0.25}\text{Sm}_{0.25})_{1-x}\text{Sr}_x\text{MnO}_3$ as a function of temperature with a measuring field of 50 Oe. a–i) The zero-field cooled (ZFC), field cooled (FC) and the derivative of the field cooled curve (dM/dT_{FC}) for all nine compositions are shown. The magnetic ground state and the main transition temperature related to the Mn–O–Mn interaction are obtained from the global minima of the dM/dT_{FC} curve. Dual magnetic transition related to the Mn–O–Mn sub-lattice is observed in (d) and (e). T_{RE} represents the secondary magnetic interactions stemming from the RE sub-lattice.

Dzyaloshinskii–Moriya interaction (DMI),^[39,40] which results in a small net ferromagnetic moment.

The M – H plots for $x = 0, 0.05, \text{ and } 0.10$ collected at various temperatures below the T_N , as shown in Figure 5 and Figure S7 (Supporting Information), indicate no sign of saturation even at high fields (7 T) and low temperatures (30 and 5 K), as is expected in the canted-AF (CAF) system. The linear, unsaturated, part of the M – H plots above T_{RE} , has two contributions, one is related to the Mn–O–Mn AFM and the other one to the paramagnetic RE cations, as mentioned earlier. The remaining saturated FM moment obtained from the M – H plots, is very small, typical of weak DMI-type ferromagnetism. Based on this combined analysis, we conclude that the ground state of $x = 0$ – 0.1 is CAF, as presented in Figure 7. Furthermore, the splitting of the FC and ZFC curves starts above the T_N indicating that the magnetic transition in HE-Mn is rather gradual occurring over a range of temperatures. The deviation from an ideal PM behavior at 100 K in $x = 0.10$, Figure S7 (Supporting Information), further confirms the gradual magnetic transition already starting above the T_N . This onset of the magnetic

ordering above the main transition temperature seems to be an effect universal to HEOs, as it has also been reported in other classes of HEOs.^[17,26,27]

The ZFC, FC, and dM/dT_{FC} data for the compositions, $x = 0.15$ and 0.20 , are shown in Figure 4d,e. Both of them exhibit two prominent magnetic transitions (denoted as T' and T_c) indicated by the abrupt change of the slope of both the FC and ZFC curves above T_{RE} , which are further supported by the dM/dT_{FC} showing minima above the T_{RE} . The main magnetic transition occurs below 90 and 103 K for $x = 0.15$ and $x = 0.20$, respectively. The magnetic state below this main transition (T_c) is expected to be of FM nature. This observation is supported by the M – H plots, exhibiting substantially higher saturated moments compared to that of the CAF systems at similar temperatures. The linear unsaturated magnetization comes largely from the RE paramagnetic moments as seen in Figure 5 and Figure S7 (Supporting Information). Based on these observations the magnetic ground states of $x = 0.15$ and $x = 0.20$ are assumed to be FM, as shown in Figure 7. Apart from this major transition, the features of the M – T curve, i.e., dM/dT_{FC} and the

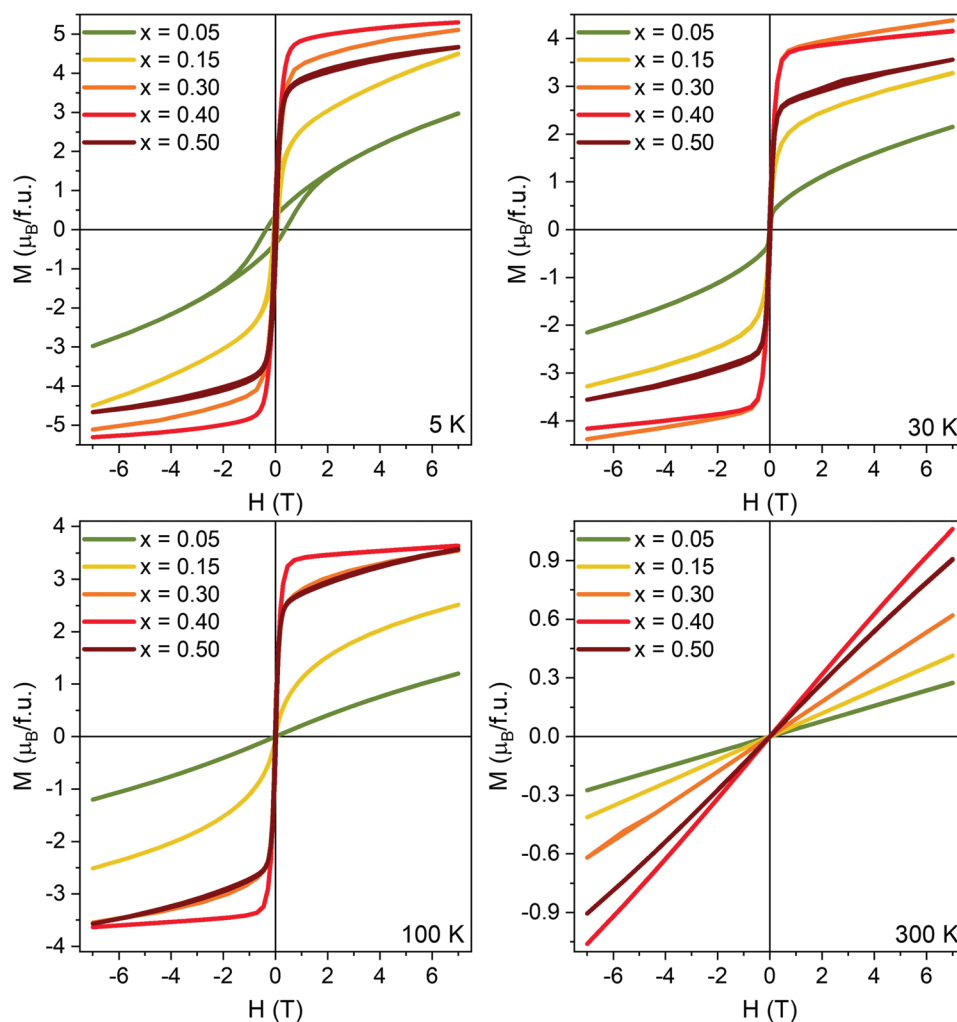


Figure 5. Magnetization of $(\text{Gd}_{0.25}\text{La}_{0.25}\text{Nd}_{0.25}\text{Sm}_{0.25})_{1-x}\text{Sr}_x\text{MnO}_3$ as a function of the field at different temperatures, 5, 30, 100, and 300 K. A linear paramagnetic behavior is observed at 300 K for all the samples. In addition, $x = 0.05$ shows a paramagnetic behavior even at 100 K, which is well above its T_N .

divergence of the ZFC and FC branches, indicate that some of the Mn spins already become magnetically ordered above the main T_c (i.e., around the T'). This is further supported by the M - H plots collected between the T_c and T' . These results provide strong hints toward inhomogeneous magnetic phase distribution in these crystallographic single-phase systems.

The aforementioned spatial magnetic inhomogeneities, also hypothesized in conventional manganites, can be explained by competing short-range SE-AF and DE-FM interactions stemming from different local ratios of Mn^{3+} and Mn^{4+} . The same can also be expected in HE-Mn. However, compared to the conventional manganites, the magnetic separation effect appears to be much more enhanced in the HE-Mn with prominent dual transitions as observed in Figure 4d,e. Hence, a different color coding is used in Figure 7 to represent the complex mixed magnetic interactions (and additional magnetic transition, T') resulting in a unique electronic behavior (more details in the next section) in these composition regimes. While the primary reason for the magnetic phase separation is still expected to be the ratio of the Mn^{3+} and Mn^{4+} , the enhancement of the phase separation can also be spurred by different-sized RE cations in

the HE-Mn. The different-sized RE cations can create a broad distribution of Mn-O-Mn bond angles resulting in a spatially fluctuating degree of Mn-O hybridization that, in turn, affects the bandwidth W . Apart from these main magnetic features, a shift in the T_{RE} toward higher temperature, ≈ 72 K, is observed even with an increased non-magnetic Sr^{2+} doping ($x = 0.15$ and 0.20) compared to the $x = 0-0.1$ compositions. The coupling T_{RE} temperature is governed by two competing factors. On the one hand, a gradual dilution of the RE ions upon doping with non-magnetic Sr weakens the coupling between RE and Mn lattices, on the other hand, Mn ferromagnetism gets stronger with more h^+ doping as the system moves from SE-AF (or CAF) toward DE-FM states. In the case of $x = 0.15$ and 0.20 , the shift of T_{RE} towards higher temperature is plausibly related to the dominant FM ordering of the Mn spins, which couple more strongly with the RE cations via the bridging oxygen compared to the weak canted moment of the Mn spins stemming from the DMI in the case of $x = 0-0.10$.

Finally, with increasing h^+ doping, $x = 0.25-0.5$, the systems exhibit a distinct PM to FM transition with high magnetic moments as indicated by the M - T , dM/dT_{FC} , and M - H plots,

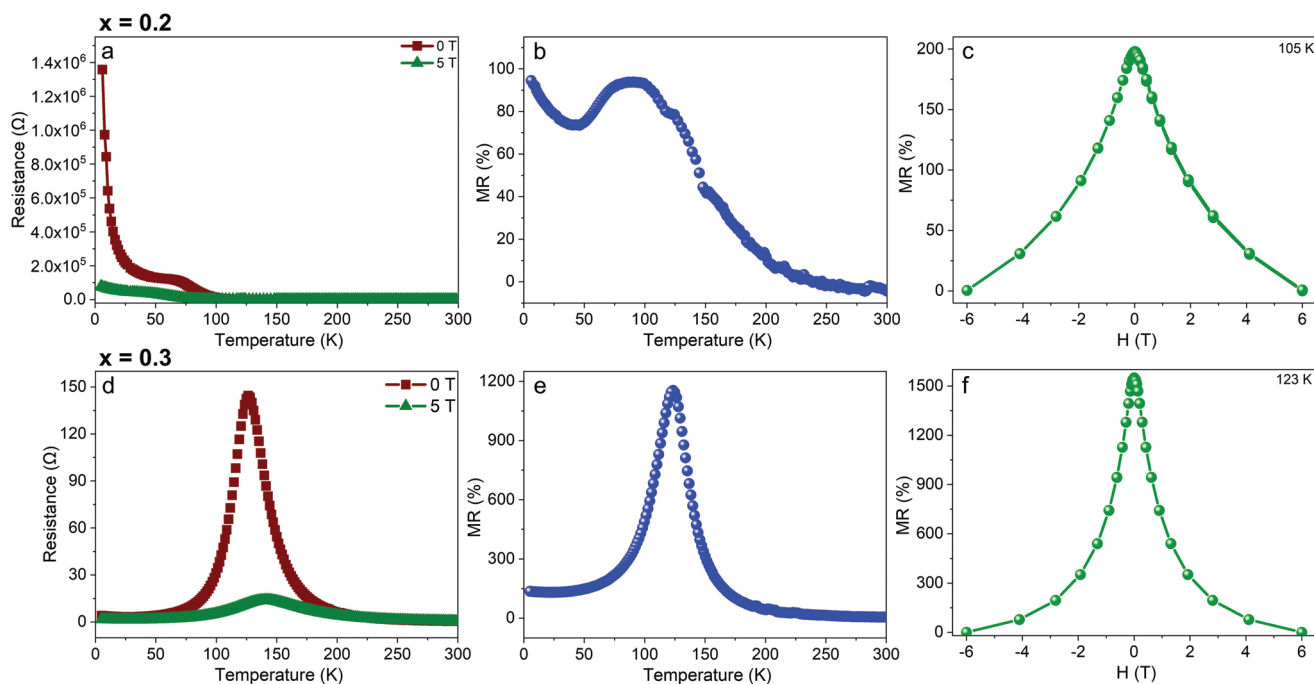


Figure 6. Magneto-electronic properties of $(\text{Gd}_{0.25}\text{La}_{0.25}\text{Nd}_{0.25}\text{Sm}_{0.25})_{0.8}\text{Sr}_{0.2}\text{MnO}_3$ (a–c) and $(\text{Gd}_{0.25}\text{La}_{0.25}\text{Nd}_{0.25}\text{Sm}_{0.25})_{0.7}\text{Sr}_{0.3}\text{MnO}_3$ (d–f). a, d) 4-probe resistance (R) measurements as a function of temperature at two different external magnetic fields (0 and 5 T) for $x = 0.2$ and $x = 0.3$, respectively, are shown. Prominent field dependency is observed in both, however, an insulating ground state is observed in $x = 0.2$ and a metal-insulator transition at the T_C in $x = 0.3$. b, e) The magneto-resistances, $MR = R_0 - R_{5T}/R_{5T}$ (in %), as the function of temperature are shown for $x = 0.2$ and $x = 0.3$, respectively. c, f) The MR (%) as the function of the external magnetic field (H) at the T_C for $x = 0.2$ and $x = 0.3$, respectively, are shown. Enhanced colossal magneto-resistance ($(R_0 - R_{6T})/R_{6T}$) of 1550% is exhibited by the $x = 0.3$ sample at 123 K.

Figures 4f–i and 5. The T_{RE} also shifts towards much lower temperatures in these systems compared to the lower doped variants, which is related to the loss of paramagnetic RE cations at higher non-magnetic Sr^{2+} doping concentrations. Below the T_C the M – H loops feature a soft, readily saturated, FM component with high magnetic moment, seen in Figure 5 (with a minor degree of linearity arising from the RE PM moments). These aforementioned results affirm the FM ground state of these compositions, $x = 0.25$ – 0.5 , as presented in Figure 7.

It can be observed that the strength of the FM interaction increases rapidly with higher h^+ doping, reflected by the high T_C for the $x = 0.4$ and 0.5 samples. However, compared to the Sr^{2+} doped variants of the constituent parent manganites, a very weak T_C temperature dependency is noticed for the compositions between $x = 0.4$ and 0.5 . For instance, the difference in the transition temperature (ΔT) between the $x = 0.4$ and $x = 0.5$ variants are roughly 20–30% for the parent RE-Mn (such as ≈ 350 to ≈ 250 K in $\text{La}_{1-x}\text{Sr}_x\text{MnO}_3$ and ≈ 125 to ≈ 100 K in the $\text{Sm}_{1-x}\text{Sr}_x\text{MnO}_3$ variants). In contrast, only a negligible difference, $\approx 2.25\%$, in the magnetic transition temperature of $x = 0.4$ (222 K) and $x = 0.5$ (217 K) is observed in the HE-Mn. Inversely, the difference in the ΔT from $x = 0.3$ to $x = 0.4$ in the parent RE-Mn is ≈ 5 – 20% , while the difference in the case of the RE-Mn is $\approx 45\%$. Furthermore, by comparing the M – H plots for $x = 0.4$ and 0.5 of HE-Mn, it can be observed that the $x = 0.5$ sample starts to show signs of magnetic inhomogeneity. This is indicated by the increase of the linear non-saturating part of the M – H plot for $x = 0.5$ (even though the paramagnetic RE constituents are reduced) and presence of hysteresis even

at higher external fields (Figure S8, Supporting Information). The origin of this magnetic inhomogeneity can be the gradual strengthening of the competing SE-AF Mn^{4+} – O – Mn^{4+} interactions over the DE-FM Mn^{3+} – O – Mn^{4+} interactions.

In summary, the HE-Mn systematically doped with Sr show a unique structural-magneto-electronic phase diagram that arises from the distinct competition between the primary magneto-electronic phases typical of the RE-manganites. The compositions $x = 0$ – 0.1 show CAF ground state, $x = 0.15$ and 0.2 show FM ground states with definitive secondary transitions at high temperatures, and $x = 0.25$ – 0.5 show a prominent single FM ground state. Differences from the parent Sr^{2+} RE-manganites are reflected in the transition temperatures and, especially, in terms of the ΔT % among the doped variants of HE-Mn. In addition, clear signs of magnetic phase separation, with prominent dual transition temperature stemming from the competing magnetic phases can be observed in the case of the HE-Mn with $x = 0.15$ and $x = 0.20$, indicating the possible use of HE design approach to enhance magnetic inhomogeneity in crystallographic single-phase manganites. Next, we evaluate magneto-transport properties of the HE-Mn.

2.2.2. Correlated Magneto-Electronic Properties and Colossal Magneto-Resistance in $(\text{Gd}_{0.25}\text{La}_{0.25}\text{Nd}_{0.25}\text{Sm}_{0.25})_{1-x}\text{Sr}_x\text{MnO}_3$

We probed the transport properties as a function of temperature (T) and external magnetic fields (H_{ext}) for three systems ($x = 0.1, 0.2$, and 0.3) exhibiting the different magnetic ground

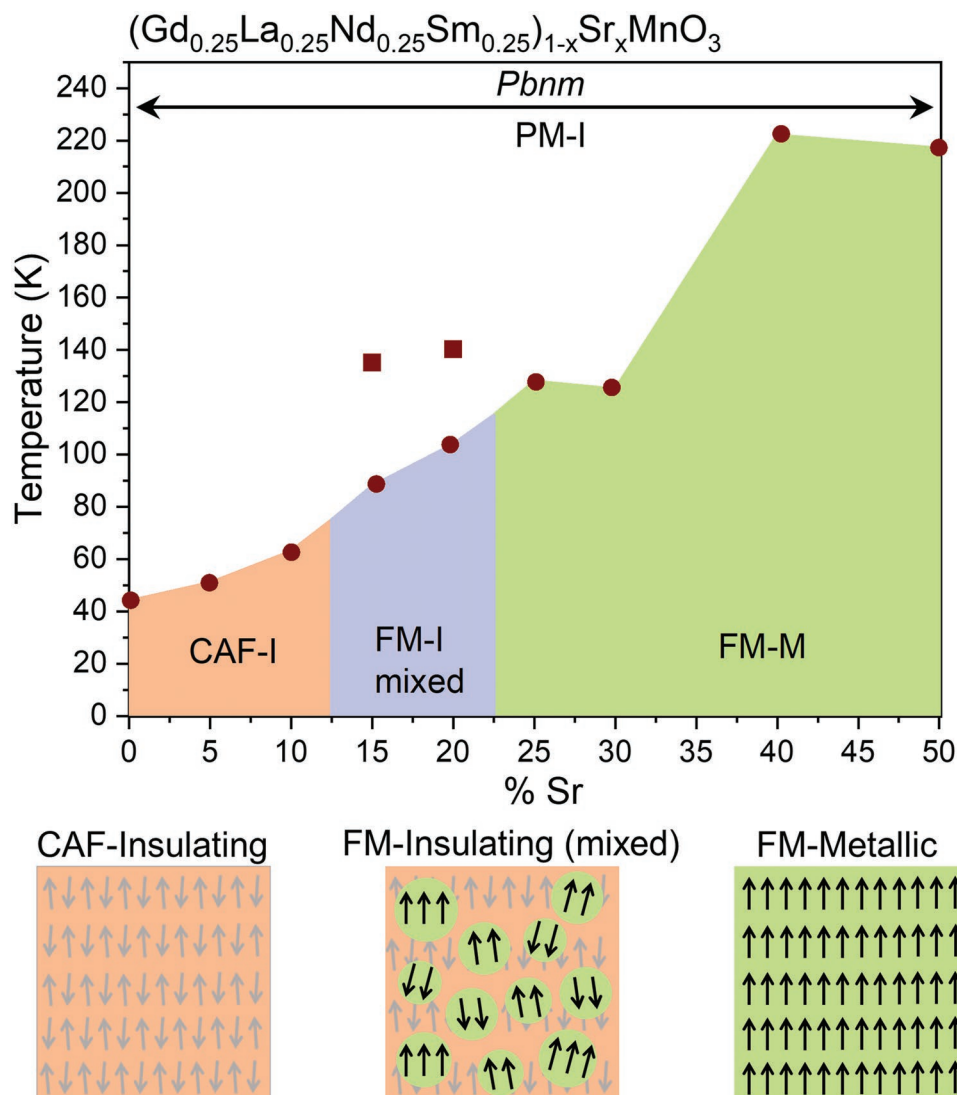


Figure 7. Magneto-electronic phase diagram of $(\text{Gd}_{0.25}\text{La}_{0.25}\text{Nd}_{0.25}\text{Sm}_{0.25})_{1-x}\text{Sr}_x\text{MnO}_3$. All systems are single-phase orthorhombic perovskites. Paramagnetic (PM) state prevails at room temperature for all compositions. Compositions $x = 0$ – 0.1 show a canted antiferromagnetic insulating (CAF-I) ground state. $x = 0.15$ and 0.20 show a ferromagnetic-insulating (FM-I) ground state with dual magnetic transitions (mixed) indicating strong magneto-electronic non-uniformity. One distinct FM-metallic (FM-M) ground state can be observed in $x = 0.25$ – 0.5 systems. Simple schematics of the obtained magneto-electronic ground states are shown below the phase diagram indicating the prohibited percolation of the metallic-FM states in systems with the FM-I mixed ground states and the long-range metallicity in the systems with the FM-M ground states.

states (CAF, FM-mixed, and FM). The resistance as a function of temperature (Ω - T) at specific H_{ext} and magnetic field-dependent magneto-resistance (MR - H) at specific temperature for $x = 0.2$ and 0.3 are shown in Figure 6.

The Ω - T for $x = 0.1$ is presented in Figure S9 (Supporting Information), which shows an exponential increase of resistance with decreasing temperature. This signifies that the system is insulating throughout the entire measured temperature regime. In fact, the resistance for the $x = 0.1$ system exceeded the limit of the PPMS (with the highest possible applicable voltage) at temperatures below 110 K and the high resistance (>10 M Ω) was retained even below the T_N (60 K). In addition, no detectable difference in the Ω - T behavior could be observed upon application of $H_{\text{ext}} = 5$ T. These results coherently support the observed CAF magnetic ground state for

$x = 0.1$, confirming the insulating SE-AF interaction in systems with $x = 0$ – 0.1 , as concluded in Figure 7.

The Ω - T data for $x = 0.2$ are shown in Figure 6a. Similar to $x = 0.1$, an exponential increase of resistance with lowering temperature could be observed almost over the entire temperature range. This indicates an insulating ground state despite the FM ordering, as presented in Figure 7. However, around the T_c (100 K), a deviation from the otherwise exponential behavior of Ω could be observed. Essentially, an obvious correlation of the electronic and magnetic properties could be observed that manifests itself through distinct lowering of Ω upon application of $H_{\text{ext}} = 5$ T at temperatures slightly below the T_c (Figure 6a). Consequently, this difference in the Ω with and without a H_{ext} results in a prominent magneto-resistance (MR) effect, as shown in Figure 6b. The MR value at the T_c

(105 K) reaches a maximum of 200%, as can be seen from the $MR-H$ plot ($H_{\text{ext}} = \pm 6$ to 0 T). It should be noted that the MR in this case and throughout the manuscript represents the $\Delta R/R_H$ (%) (more details in the experimental section), which is the widely followed convention. However, the MR is also often represented as $\Delta R/R_0$ (%) or as the R_0/R_H (see experimental section for details). The corresponding $\Delta R/R_0$ and R_0/R_H for $x = 0.2$ at 105 K are 67% and 3, respectively. These observations concordantly support the coexistence of two different magneto-electronic ground states for $x = 0.2$, as concluded from the magnetometry data.

Thus, it can be concluded that the system $x = 0.2$ exhibits a competition between the insulating SE-AFM and metallic DE-FM interactions. Unlike, the $x = 0.1$ system with the CAF ground state, the DE-FM interactions are dominant resulting in the aforementioned magnetic features, like high magnetic moments in $x = 0.2$. However, the SE-AFM interaction resists the percolation of the long-ranged metallic DE-FM interactions throughout the system, as shown in the schematics of the magneto-electronic ground states in Figure 7. In fact, the percolation of the metallic interactions ($x = 0.2$) could not be obtained even at 5 T (Figure 6a) portraying the robustness of the insulating AF matrix separating the metallic-FM clusters. Furthermore, a high and almost consistent value of MR can be observed over a wide temperature range already starting well above the T_C (Figure 6b,c). These effects of a magneto-electronic phase separation and a gradual magneto-electronic phase transition can plausibly stem from the highly disordered A-site, resulting in locally varying Mn–O–Mn bond angles.

Finally, we probe the $(\text{Gd}_{0.25}\text{La}_{0.25}\text{Nd}_{0.25}\text{Sm}_{0.25})_{0.7}\text{Sr}_{0.3}\text{MnO}_3$ as a representative of the FM ground state. The $\Omega-T$ behavior with and without H_{ext} differ substantially from both the insulating-CAF and insulating-FM mixed ground states (Figure 6d,e). A definitive MIT occurs at 123 K (Figure 6d,e),

which is identical to the T_C . Above the T_C the Ω decreases with increasing T indicating an insulating state, while below the T_C the system exhibits a metallic behavior as the Ω decreases with decreasing T . This affirms the metallic DE-FM interaction in $x = 0.3$, as shown in Figure 7. Furthermore, the maximum value of the MR observed at 123 K is $\approx 1550\%$ ($H_{\text{ext}} = \pm 6$ T to 0 T) as can be seen in Figure 6f. The corresponding $\Delta R/R_0$ and R_0/R_H values at 123 K are 94% and 16.5, respectively. These respective values are comparable to the best-known CMR effects reported for bulk manganite polycrystalline pellets and exceed the parent $\text{RE}_{1-x}\text{A}_x\text{MnO}_3$ ($A = \text{Sr}$ or Ca) around and >100 K.^[2,41–46] **Table 1** compares the MR values of different parent variants of bulk polycrystalline $\text{RE}_{1-x}\text{Sr}_x\text{MnO}_3$ with that obtained for the HE-Mn.

As mentioned earlier, the CMR effect relies on magneto-electronic inhomogeneity, which is plausibly enhanced by the chemically disordered A-site resulting in the substantial CMR already in an unoptimized polycrystalline pellet. These initial results highlight the potential for further improvement of the CMR effect, using conventional design approaches followed in conventional manganites, like strained thin film deposition, single crystal growth, variation in oxygen stoichiometry, etc. For instance, one of the highest known CMR effects is observed in a single crystal thin film of $\text{La}_{1-x}\text{Ca}_x\text{MnO}_3$, where an improvement in CMR from $\approx 500\%$ to $\approx 127\,000\%$ could be achieved via straining and alteration of oxygen stoichiometry.^[47] The CMR values of the $\text{La}_{0.7}\text{Ca}_{0.3}\text{MnO}_3$ and $\text{Nd}_{0.7}\text{Sr}_{0.3}\text{MnO}_3$, which are amongst the highest known,^[47,48] are presented in Table 1 for comparison. It can be observed that the MR values ($\Delta R/R_0$) of the bulk polycrystalline pellets of $\text{La}_{0.7}\text{Ca}_{0.3}\text{MnO}_3$ (55%) and $\text{Nd}_{0.7}\text{Sr}_{0.3}\text{MnO}_3$ (80%) are lower than the 30% h^+ doped HE-Mn variant, $(\text{Gd}_{0.25}\text{La}_{0.25}\text{Nd}_{0.25}\text{Sm}_{0.25})_{0.7}\text{Sr}_{0.3}\text{MnO}_3$ (94%). This highlights the possibility of manipulation and enhancement of the CMR of the HE-Mn for instance with strained thin-film deposition. In addition, future investigation with hole doping

Table 1. The MR values, represented either in $\Delta R/R_H$ (%) or $\Delta R/R_0$ (%), of different conventional bulk polycrystalline variants of Sr doped RE-manganite are compared with the HE-Mn. Additionally, thin film and Ca doped variants of RE-manganite known for their high degree of MR are shown. H_{max} is the maximum external magnetic field used for the MR, while the T_{MR} represents the temperature where the maximum MR is observed.

Compositions	$\Delta R/R_H$ [%]	$\Delta R/R_0$ [%]	T_{MR} [K]	H_{max}	Ref.
$\text{La}_{0.8}\text{Sr}_{0.2}\text{MnO}_3$	–	46	270	6T	[51]
$\text{Nd}_{0.8}\text{Sr}_{0.2}\text{MnO}_3$	–	88	70	8T	[45]
$(\text{Gd}_{0.25}\text{La}_{0.25}\text{Nd}_{0.25}\text{Sm}_{0.25})_{0.8}\text{Sr}_{0.2}\text{MnO}_3$	10^2	67	105^a	6T	This work
$\text{La}_{0.7}\text{Sr}_{0.3}\text{MnO}_3$	–	45	330	6T	[51]
$\text{La}_{0.7}\text{Sr}_{0.3}\text{MnO}_3$ (thin film)	–	68	330	9T	[31]
$\text{Nd}_{0.67}\text{Sr}_{0.33}\text{MnO}_3$	–	51	260	6T	[52]
$\text{Nd}_{0.7}\text{Sr}_{0.3}\text{MnO}_3$	–	80	100	9T	[53]
$\text{Nd}_{0.7}\text{Sr}_{0.3}\text{MnO}_3$ (thin film)	10^5	–	70	7T	[48]
$\text{Sm}_{0.7}\text{Sr}_{0.3}\text{MnO}_3$	10^2	–	125	5T	[54]
$\text{Nd}_{0.33}\text{Sm}_{0.34}\text{Sr}_{0.33}\text{MnO}_3$	–	71	190	7T	[52]
$\text{Nd}_{0.33}\text{Gd}_{0.34}\text{Sr}_{0.33}\text{MnO}_3$	–	90	145	7T	[52]
$\text{La}_{0.30}\text{Gd}_{0.36}\text{Sr}_{0.33}\text{MnO}_3$	10^3	–	118	4T	[55]
$\text{La}_{0.7}\text{Ca}_{0.3}\text{MnO}_3$	–	55	260	6T	[51]
$\text{La}_{0.7}\text{Ca}_{0.3}\text{MnO}_3$ (thin film)	10^6	–	77	6T	[47]
$(\text{Gd}_{0.25}\text{La}_{0.25}\text{Nd}_{0.25}\text{Sm}_{0.25})_{0.7}\text{Sr}_{0.3}\text{MnO}_3$	10^3	94	123	6T	This work

^aPercolation could not be reached at the maximum field.

achieved via Ca instead of Sr, allowing substantial change in W , will be another way to enhance CMR effect in HE-Mn. Likewise, altering the relative concentration of the A-site RE cations, that is deviating from the complete equiatomicity, or substituting some of them with other RE-cations (like mixed valent Pr, Tb, or Ce), will result in a change in W , as well as the Mn-band filling. Hence, composition modulation will affect the strongly correlated functionalities of HE-Mn. Nevertheless, given the vast composition space of HE-Mn, like in any other HE-materials, high-throughput-based experimental methods, supported by machine learning and theoretical predictions,^[49] will be crucial for optimizing the functionalities of HE-Mn.

3. Conclusions

This study demonstrates a new way to tailor strongly correlated functionalities in oxide systems based on the high entropy (HE) design approach. Nine high entropy manganites (HE-Mn), $(\text{Gd}_{0.25}\text{La}_{0.25}\text{Nd}_{0.25}\text{Sm}_{0.25})_{1-x}\text{Sr}_x\text{MnO}_3$, with varying amounts of Sr^{2+} (h^+) dopant, $x = 0, 0.05, 0.1, 0.15, 0.20, 0.25, 0.30, 0.40$, and 0.50 , are stabilized as phase-pure orthorhombic perovskites with homogenous distribution of the cations over their respective sub-lattices. HR-TEM studies performed on a single phase HE-Mn with $x = 0.5$ reveal the presence of three different kinds of hitherto unknown lattice imperfections in high entropy oxides: twins, stacking faults, and missing planes.

The magnetic and electronic studies highlight a complex magneto-electronic phase diagram with unique temperature dependencies that stem from competing magneto-electronic interactions. At a lower doping level ($x = 0-0.1$) a predominant asymmetric superexchange (SE) interaction prevails resulting in an insulating canted-antiferromagnetic (CAF) state. Intermediate doping (in the $x = 0.15$ and 0.2 regimes) exhibits signatures of magneto-electronic phase separation arising from a competition of insulating-SE and metallic-double-exchange (DE) ferromagnetic (FM) interactions. Well-defined multiple magnetic transitions indicate the enhanced magneto-electronic inhomogeneity in HE-Mn. The magnetism in these systems ($x = 0.15$ and 0.2) is governed by the metallic-FM clusters separated by the insulating-AF matrix. Even though the FM clusters do not reach a percolation threshold, the systems respond to the external magnetic field resulting in the colossal magneto-resistance (CMR) effect of $\approx 200\%$ at T_c . Finally, at the increased h^+ doping a robust long-range metallic-DE-FM prevails. Correspondingly, a metal-insulator transition at T_c with a substantial degree of the CMR effect $\approx 1550\%$ is observed. Such a CMR value obtained on a polycrystalline pellet is already comparable to the best-known results in this temperature range for bulk manganite samples, surpassing the parent Sr doped RE-manganites. Consequently, building on the proposed design concept, further improvements in the material performance can be expected via A-site composition modulation, microstructural modifications, oxygen stoichiometry tailoring, and (strained) thin film deposition. Overall, this initial study signals excellent potential for new research opportunities offered by the merger of the high-entropy-based design approach with the strongly correlated electron systems.

4. Experimental Section

Materials Synthesis: The powder samples were synthesized using nebulized spray pyrolysis (NSP) method. The details of the synthesis procedure can be found elsewhere.^[50] A total of nine samples were synthesized with 0%, 10%, 15%, 20%, 25%, 30%, 40%, and 50% of the RE elements substituted by Sr, with the corresponding chemical formula $(\text{Gd}_{0.25}\text{La}_{0.25}\text{Nd}_{0.25}\text{Sm}_{0.25})_{1-x}\text{Sr}_x\text{MnO}_3$ where $x = 0, 0.05, 0.1, 0.15, 0.20, 0.25, 0.30, 0.40$, and 0.50 , respectively. Aqueous-based precursor solutions with a concentration of 0.1 mol l^{-1} were prepared by dissolving stoichiometric amounts of nitrate salts of the corresponding metal cations, $\text{Gd}(\text{NO}_3)_3 \cdot 6\text{H}_2\text{O}$, $\text{La}(\text{NO}_3)_3 \cdot 6\text{H}_2\text{O}$, $\text{Nd}(\text{NO}_3)_3 \cdot 6\text{H}_2\text{O}$, $\text{Sm}(\text{NO}_3)_3 \cdot 6\text{H}_2\text{O}$, $\text{Mn}(\text{NO}_3)_3 \cdot 4\text{H}_2\text{O}$, $\text{Sr}(\text{NO}_3)_2$, in water. The mist of the precursor solution generated from the piezo-driven nebulizer was transported to the hot-wall reactor using N_2 as the carrier gas (3 standard liters per minute). The hot-wall reactor was maintained at a temperature of $1000 \text{ }^\circ\text{C}$ and a pressure of 900 mbar . The as-synthesized powders were collected using a filter-based collector and calcined at $1200 \text{ }^\circ\text{C}$ for 2.5 h in air atmosphere with a heating and cooling rate of $10 \text{ }^\circ\text{C min}^{-1}$. These calcined samples are used for further characterizations. For magneto-resistance measurements, $\approx 90\%$ dense sintered pellets with 8 mm diameter were used, which were prepared by pressing the powders at 200 MPa uniaxial pressure followed by sintering in air atmosphere at $1300 \text{ }^\circ\text{C}$ for 24 h .

X-Ray Diffraction: Room temperature XRD patterns of the powder samples were recorded using a Bruker D8 Advance with Bragg-Brentano geometry using $\text{Cu-K}\alpha$ radiation with a Ni filter and a LYNXEYE detector having a fixed divergence slit (0.3°). A step size of 0.02° and a collection time of 4 s per step at 30 kV and 40 mA over the diffraction angle (2θ) range between 10 and 90° were used. Rietveld analysis of the XRD patterns was performed using TOPAS V.7. (Academic version) to determine the structure and phase composition of the powders. The instrumental intensity distribution for the XRD data was determined using a reference scan of LaB6 (NIST 660a). Thermal displacement parameters were constrained to be the same for all atoms.

High-Resolution Transmission Electron Microscopy (HR-TEM), Electron Energy Loss Spectroscopy (EELS), and Energy Dispersive Spectroscopy: A double aberration corrected state-of-the-art Themis Z (Thermo Fisher) HR-TEM equipped with a Super-X energy dispersive X-ray detector and Gatan GIF Continuum 970 HighRes + K3 IS camera (operated at 300 kV) were used to examine the specimens. EELS spectrum presented is the average of at least 15 spectra collected from different regions of samples, likewise the HR-TEM and HR-STEM micrographs were taken from different regions to confirm the large-scale homogeneity of the samples.

X-Ray Photoelectron Spectroscopy: XPS measurements were performed using a K-Alpha XPS spectrometer (ThermoFisher Scientific, East Grinstead, UK). For data acquisition and processing, the Thermo Avantage software was used. All samples were analyzed using a microfocused, monochromated $\text{Al K}\alpha$ X-ray source ($400 \text{ }\mu\text{m}$ spot size). The K-Alpha charge compensation system was employed during analysis, using electrons of 8 eV energy, and low-energy argon ions to prevent any localized charge build-up. The spectra were fitted with one or more Voigt profiles (uncertainty in the binding energy: $\pm 0.2 \text{ eV}$). All spectra were referenced to the $\text{C } 1 \text{ s}$ peak (C-C, C-H) at 285.0 eV binding energy.

Magnetometry and Magneto-Electronic Measurements: Magnetic measurements at room temperature were performed on the powder samples using a Quantum Design MPMS3 superconducting quantum interference device (SQUID) in vibrating sample magnetometer (VSM) mode. The magneto-transport properties were studied on sintered pellets using a Quantum Design physical properties measurement system (PPMS) using a 4-point measurement technique. It should be noted that all magneto-electronic measurements for a given system were collected at once, i.e., using the same sample and connections, to make sure that the obtained resistances can be precisely compared. The magnetoresistance (MR) used in Figure 7 was calculated using Equations 2 and 3, where R_0 and R_H are the resistance without field

(0 T) and the highest field (5 T for Figure 6b,e or 6 T for Figure 6c,f), respectively:

$$MR = \frac{\Delta R}{R_H} \quad (2)$$

$$\Delta R = R_0 - R_H \quad (3)$$

Although the representation of MR using Equation 2 is the most widely followed approach, there are several reports where alternate relations are used to represent the magnetoresistance, $\Delta R/R_0$ and R_0/R_H .

Supporting Information

Supporting Information is available from the Wiley Online Library or from the author.

Acknowledgements

A.S. and H.H. acknowledge financial support from the Deutsche Forschungsgemeinschaft (DFG) project HA 1344/43-2. KMV acknowledges DAAD-IIT Master Sandwich program 2019–20. The authors thank the Karlsruhe Nano Micro Facility (KNMFi, Germany) for providing access to the TEM and XPS facilities.

Open access funding enabled and organized by Projekt DEAL.

Conflict of Interest

The authors declare no conflict of interest.

Data Availability Statement

The data that support the findings of this study are available from the corresponding author upon reasonable request.

Keywords

colossal magnetoresistance, high entropy oxides, magneto-electronic phase separation, metal-insulator transitions, strongly correlated electron systems

Received: August 15, 2022

Revised: November 4, 2022

Published online:

- [1] E. Dagotto, *Science* **2005**, 309, 257.
 [2] Y. Tokura, *Rep. Prog. Phys.* **2006**, 69, 797.
 [3] M. Uehara, S. Mori, C. H. Chen, S.-W. Cheong, *Nature* **1999**, 399, 560.
 [4] E. Dagotto, T. Hotta, A. Moreo, *Phys. Rep.* **2001**, 344, 1.
 [5] P. W. Anderson, H. Hasegawa, *Phys. Rev.* **1955**, 100, 675.
 [6] J. B. Goodenough, *Phys. Rev.* **1955**, 100, 564.
 [7] H. Röder, J. Zang, A. R. Bishop, *Phys. Rev. Lett.* **1996**, 76, 1356.
 [8] Y. Tokura, *Science* **2006**, 312, 1481.
 [9] J. Hemberger, A. Krimmel, T. Kurz, H.-A. Krug von Nidda, V. Y. Ivanov, A. A. Mukhin, A. M. Balbashov, A. Loidl, *Phys. Rev. B* **2002**, 66, 094410.

- [10] V. Moshnyaga, B. Damaschke, O. Shapoval, a Belenchuk, J. Faupel, O. I. Lebedev, J. Verbeeck, G. van Tendeloo, M. Mücksch, V. Tsurkan, R. Tidecks, K. Samwer, *Nat. Mater.* **2003**, 2, 247.
 [11] A. Sarkar, Q. Wang, A. Schiele, M. R. Chellali, S. S. Bhattacharya, D. Wang, T. Brezesinski, H. Hahn, L. Velasco, B. Breitung, *Adv. Mater.* **2019**, 31, 1806236.
 [12] C. Oses, C. Toher, S. Curtarolo, *Nat. Rev. Mater.* **2020**, 5, 295.
 [13] A. Sarkar, B. Breitung, H. Hahn, *Scr. Mater.* **2020**, 187, 43.
 [14] B. Gludovatz, A. Hohenwarter, D. Catoor, E. H. Chang, E. P. George, R. O. Ritchie, *Science* **2014**, 345, 1153.
 [15] Z. Li, K. G. Pradeep, Y. Deng, D. Raabe, C. C. Tasan, *Nature* **2016**, 534, 227.
 [16] C. M. Rost, E. Sacht, T. Borman, A. Moballeggh, E. C. Dickey, D. Hou, J. L. Jones, S. Curtarolo, J.-P. Maria, *Nat. Commun.* **2015**, 6, 8485.
 [17] M. P. Jimenez-Segura, T. Takayama, D. Bérardan, A. Hoser, M. Reehuis, H. Takagi, N. Dragoe, *Appl. Phys. Lett.* **2019**, 114, 122401.
 [18] S. K. Nemani, B. Zhang, B. C. Wyatt, Z. D. Hood, S. Manna, R. Khaledialidusti, W. Hong, M. G. Sternberg, S. K. R. S. Sankaranarayanan, B. Anasori, *ACS Nano* **2021**, 15, 12815.
 [19] A. Sarkar, L. Velasco, D. Wang, Q. Wang, G. Talasila, L. de Biasi, C. Kübel, T. Brezesinski, S. S. Bhattacharya, H. Hahn, B. Breitung, *Nat. Commun.* **2018**, 9, 3400.
 [20] Z. Lun, B. Ouyang, D.-H. Kwon, Y. Ha, E. E. Foley, T.-Y. Huang, Z. Cai, H. Kim, M. Balasubramanian, Y. Sun, J. Huang, Y. Tian, H. Kim, B. D. McCloskey, W. Yang, R. J. Clément, H. Ji, G. Ceder, *Nat. Mater.* **2021**, 20, 214.
 [21] H. Xu, Z. Zhang, J. Liu, C. L. Do-Thanh, H. Chen, S. Xu, Q. Lin, Y. Jiao, J. Wang, Y. Wang, Y. Chen, S. Dai, *Nat. Commun.* **2020**, 11, 3908.
 [22] Q. Wang, L. Velasco, B. Breitung, V. Presser, *Adv. Energy Mater.* **2021**, 11, 2102355.
 [23] P. Edalati, Q. Wang, H. Razavi-Khosroshahi, M. Fuji, T. Ishihara, K. Edalati, *J. Mater. Chem. A* **2020**, 8, 3814.
 [24] J. Patra, T. X. Nguyen, C. Tsai, O. Clemens, J. Li, P. Pal, W. K. Chan, C. Lee, H. T. Chen, J. Ting, J. Chang, *Adv. Funct. Mater.* **2022**, 32, 2110992.
 [25] R. Banerjee, S. Chatterjee, M. Ranjan, T. Bhattacharya, S. Mukherjee, S. S. Jana, A. Dwivedi, T. Maiti, *ACS Sustainable Chem. Eng.* **2020**, 8, 17022.
 [26] R. Witte, A. Sarkar, R. Kruk, B. Eggert, R. A. Brand, H. Wende, H. Hahn, *Phys. Rev. Mater.* **2019**, 3, 034406.
 [27] A. Sarkar, R. Kruk, H. Hahn, *Dalton Trans.* **2021**, 50, 1973.
 [28] A. R. Mazza, E. Skoropata, Y. Sharma, J. Lapano, T. W. Heitmann, B. L. Musico, V. Keppens, Z. Gai, J. W. Freeland, T. R. Charlton, M. Brahlek, A. Moreo, E. Dagotto, T. Z. Ward, *Adv. Sci.* **2022**, 9, 2200391.
 [29] L. Su, H. Huyan, A. Sarkar, W. Gao, X. Yan, C. Addiego, R. Kruk, H. Hahn, X. Pan, *Nat. Commun.* **2022**, 13, 2358.
 [30] A. Sarkar, R. Djenadic, D. Wang, C. Hein, R. Kautenburger, O. Clemens, H. Hahn, *J. Eur. Ceram. Soc.* **2018**, 38, 2318.
 [31] L. Cao, O. Petravic, P. Zakalek, A. Weber, U. Rücker, J. Schubert, A. Koutsoubas, S. Mattauch, T. Brückel, *Adv. Mater.* **2019**, 31, 1806183.
 [32] Y. Shi, N. Ni, Q. Ding, X. Zhao, *J. Mater. Chem. A* **2022**, 10, 2256.
 [33] Z. Li, M. Bosman, Z. Yang, P. Ren, L. Wang, L. Cao, X. Yu, C. Ke, M. B. H. Breese, A. Rusydi, W. Zhu, Z. Dong, Y. L. Foo, *Adv. Funct. Mater.* **2012**, 22, 4312.
 [34] P. Rajak, D. Knez, S. K. Chaluvadi, P. Orgiani, G. Rossi, L. Méchin, R. Ciancio, *ACS Appl. Mater. Interfaces* **2021**, 13, 55666.
 [35] Y. Han, X. Liu, Q. Zhang, M. Huang, Y. Li, W. Pan, P. Zong, L. Li, Z. Yang, Y. Feng, P. Zhang, C. Wan, *Nat. Commun.* **2022**, 13, 2871.
 [36] F. Masee, S. de Jong, Y. Huang, W. K. Siu, I. Santoso, A. Mans, A. T. Boothroyd, D. Prabhakaran, R. Follath, A. Varykhalov, L. Patthey, M. Shi, J. B. Goedkoop, M. S. Golden, *Nat. Phys.* **2011**, 7, 978.

- [37] R. Seshadri, M. Hervieu, C. Martin, A. Maignan, B. Domenges, B. Raveau, A. N. Fitch, *Chem. Mater.* **1997**, *9*, 1778.
- [38] M. A. Hossain, M. H. Burkhardt, S. Sarkar, H. Ohldag, Y.-D. Chuang, A. Scholl, A. T. Young, A. Doran, D. S. Dessau, H. Zheng, J. F. Mitchell, H. A. Dürr, J. Stöhr, *Appl. Phys. Lett.* **2012**, *101*, 132402.
- [39] I. Dzyaloshinsky, *J. Phys. Chem. Solids* **1958**, *4*, 241.
- [40] T. Moriya, *Phys. Rev.* **1960**, *120*, 91.
- [41] B. Raveau, A. Maignan, C. Martin, M. Hervieu, *Chem. Mater.* **1998**, *10*, 2641.
- [42] Q. Song, G. Wang, G. Yan, Q. Mao, W. Wang, Z. Peng, *J. Rare Earths* **2008**, *26*, 821.
- [43] Y. Huang, S. Wang, F. Luo, S. Jiang, C. Yan, *Chem. Phys. Lett.* **2002**, *362*, 114.
- [44] A. I. Abramovich, A. V. Michurin, O. Y. Gorbenko, A. R. Kaul, *J. Phys. Condens. Matter.* **2000**, *12*, L627.
- [45] S. Kundu, T. K. Nath, *J. Phys. Condens. Matter.* **2011**, *23*, 356001.
- [46] A. de Andrés, M. García-Hernández, J. L. Martínez, *Phys. Rev. B* **1999**, *60*, 7328.
- [47] S. Jin, T. H. Tiefel, M. McCormack, R. A. Fastnacht, R. Ramesh, L. H. Chen, *Science* **1994**, *264*, 413.
- [48] G. C. Xiong, Q. Li, H. L. Ju, S. N. Mao, L. Senapati, X. X. Xi, R. L. Greene, T. Venkatesan, *Appl. Phys. Lett.* **1995**, *66*, 1427.
- [49] L. Velasco, J. S. Castillo, M. V. Kante, J. J. Olaya, P. Friederich, H. Hahn, *Adv. Mater.* **2021**, *33*, 2102301.
- [50] A. Sarkar, R. Djenadic, N. J. Usharani, K. P. Sanghvi, V. S. K. Chakravadhanula, A. S. Gandhi, H. Hahn, S. S. Bhattacharya, *J. Eur. Ceram. Soc.* **2017**, *37*, 747.
- [51] R. Mahendiran, S. K. Tiwary, A. K. Raychaudhuri, T. V. Ramakrishnan, R. Mahesh, N. Rangavittal, C. N. R. Rao, *Phys. Rev. B* **1996**, *53*, 3348.
- [52] K. Padmavathi, G. Venkataiah, P. Venugopal Reddy, *J. Magn. Magn. Mater.* **2007**, *309*, 237.
- [53] C. Krishnamoorthy, K. Sethupathi, V. Sankaranarayanan, R. Nirmala, S. K. Malik, *J. Nanopart. Res.* **2007**, *9*, 765.
- [54] C.-H. Yan, F. Luo, Y.-H. Huang, X.-H. Li, Z.-M. Wang, C.-S. Liao, H.-W. Zhao, B.-G. Shen, *J. Appl. Phys.* **2002**, *91*, 7406.
- [55] X. Cui, X. Hu, H. Xia, J. Yu, D. Wang, S. Zhang, *J. Mater. Sci.* **2005**, *40*, 5053.